Modeling photonic force microscopy with metallic particles under plasmon eigenmode excitation

J. R. Arias-González,[1] M. Nieto-Vesperinas,[1,*] and M. Lester[2]
[1]*Instituto de Ciencia de Materiales de Madrid, Consejo Superior de Investigaciones Científicas, Campus de Cantoblanco, 28049 Madrid, Spain*
[2]*Instituto de Física Arroyo Seco, Facultad de Ciencias Exactas, Universidad Nacional del Centro de la Provincia de Buenos Aires, Pinto 399 (7000) Tandil, Argentina*

(Received 14 June 2001; revised manuscript received 27 September 2001; published 15 February 2002)

The photonic force microscopy is a scanning technique of imaging surface topography at the nanometrical scale that was recently modeled. In this work, metallic probes are studied either on or off probe particle plasmon resonance excitation. A comparison with silicon particles, where morphology-dependent resonances take place, is done. The force signal is also analyzed and compared to well-known (constant distance) near-field microscopy techniques. The results show that photonic force microscopy provides a better image of surface topography at nanometric scale when the plasmon eigenmodes are excited in the metallic probe.

DOI: 10.1103/PhysRevB.65.115402 PACS number(s): 78.70.−g, 03.50.De, 07.79.−v, 73.20.Mf

I. INTRODUCTION

Dielectric particles suffer intensity gradient forces under light illumination due to radiation pressure, that permits to hold and manipulate them by means of optical tweezers[1] in a variety of techniques such as spectroscopy,[2–4] phase transitions in polymer molecules,[5] and light force microscopy of cells[6,7] and biomolecules.[8]

Metallic particles, however, were initially reported to suffer repulsive electromagnetic scattering forces due to their higher cross sections,[9] although later[10] it was shown that nanometric metallic particles (with diameters smaller than 50 nm) can be held in an optical tweezer focused in the focal region of a laser beam. Further, it was demonstrated in an experiment[11] that metallic particles illuminated by an evanescent wave created under total internal reflection at a substrate, experience a vertical attractive force towards the plate, while they are pushed horizontally in the direction of propagation of the evanescent wave along the surface. Forces in the fN range were measured. Thus, this trapped particle method constitutes a way to measure extremely small forces. Being more sensitive than conventional AFM (atomic force microscopy) devices, since the trap spring constants are 3 or 4 orders of magnitude smaller than AFM cantilevers.[12]

Three-dimensional calculations and experiments of forces on microparticles on flat substrates, apertures, and close to fiber tips in near-field optical microscopy have been carried out.[13–27]

In this paper, we show that those effects combined permit to get through the force signal transduction, an image of a corrugated dielectric surface topography by using the particle scanning above it. We shall also show that this procedure is particularly effective when illumination is done at wavelengths that excite the plasmon eigenmodes of the particle.[28] In this case the optical force exerted on the particle is enhanced, and the attractive vertical force presents a higher signal with contrast reversed with respect to that of the surface topography. We show that this reversal is related to the decrease of the vertical attractive force with the distance between the particle and the substrate. After a brief introduction in Sec. II, we present numerical results for small particles in Sec. III A. Comparisons with the force signal obtained from dielectric particles are carried out. Then, in Sec. III B, we discuss the situation of particles that present a larger cross section and thus on which there exists a competition between gradient and scattering forces.

For reasons of computer memory and time, calculations will be done in two dimensions (2D). This configuration contains, however, the main physical effects of the 3D system, as regards multiple scattering field and forces on interaction between the particle and the interface.[26]

II. FORMULATION

Figure 1 illustrates the geometry under study: a nanometrical cylinder (the 2D version of a particle) immersed in water ($\epsilon_0 = 1.7769$) scans a water-glass interface with relief defects ($\epsilon_1 = 2.3104$). An incident Gaussian beam of half width at half maximum W, either S or P polarized, namely, with the electric or magnetic vector along the Y axis, respectively, illuminates from the glass side at angle θ_0. Since the configuration is 2D, the incident power and the force are expressed in W/nm and N/nm, respectively, namely, as power and force magnitudes per unit length (in nm) in the transversal direction, i.e., that of the cylinder axis. Our aim is to study the electromagnetic forces acting on the nanocylinder under total internal reflection (TIR) illumination condi-

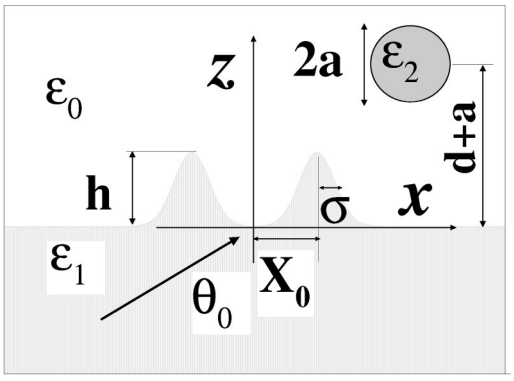

FIG. 1. Geometry of the system.

tions, so that θ_0 be larger than the critical angle $\theta_c = 61.28°$. Multiple interactions of the scattered wave between the object and the rough surface are fully taken into account. Silver cylinders of radius a at distance $d+a$ from the flat portion of the surface are addressed. The profile that has been considered consists of two protrusions on a flat interface described by the height, $z=h\{\exp[-(x-X_0)^2/\sigma^2] + \exp[-(x+X_0)^2/\sigma^2]\}$, as shown in Fig. 1. For this configuration there is no depolarization in the scattering of either *S* or *P* waves. The incident electric and magnetic vectors are, respectively,

$$\mathbf{E}_0(\mathbf{r},t)=[0,\Phi_s^{(inc)}(\mathbf{r}),0]\exp(-i\omega t), \tag{1}$$

$$\mathbf{H}_0(\mathbf{r},t)=[0,\Phi_p^{(inc)}(\mathbf{r}),0]\exp(-i\omega t), \tag{2}$$

where

$$\Phi_\alpha^{(inc)}(\mathbf{r})=\exp[ik_0(x\sin\theta_0+z\cos\theta_0)g(x,z)] \times\exp[-(x\cos\theta_0-z\sin\theta_0)^2/W^2], \tag{3}$$

$k_0=2\pi/\lambda$, λ being the wavelength in vacuum; α standing for either *s* or *p*, and

$$g(x,z)=1+\frac{1}{k_0^2W^2}\left[\frac{2}{W^2}(x\cos\theta_0-z\sin\theta_0)^2-1\right], \tag{4}$$

The field is rigorously calculated by means of the extinction theorem boundary condition.[29–33] The electromagnetic forces are then obtained from Maxwell's stress tensor.[26,34] At optical frequencies involved in many experiments, however, only the time average of the electromagnetic force is observed. This averaged force on a particle embedded in an isotropic medium is

$$\langle\mathbf{F}\rangle=1/(8\pi)\mathrm{Re}\left[\int_S[(\epsilon\mathbf{E}(\mathbf{r},\omega)\cdot\mathbf{n})\mathbf{E}^*(\mathbf{r},\omega) + (\mu\mathbf{H}(\mathbf{r},\omega)\cdot\mathbf{n})\mathbf{H}^*(\mathbf{r},\omega)-1/2(\epsilon|\mathbf{E}(\mathbf{r},\omega)|^2 + \mu|\mathbf{H}(\mathbf{r},\omega)|^2)\mathbf{n}]d\mathbf{r}\right], \tag{5}$$

where S is a surface enclosing the particle, **n** stands for the local outward unit normal, * denotes the complex conjugate, and Re represents the real part of a complex number. Let us notice that Eq. (5) is written in C.G.S. units. For our 2D scheme, we shall integrate along the boundary line of the geometrical cross section of the cylinder, thus we will present the force magnitude per unit length.

III. NUMERICAL RESULTS

Figure 2 shows the extinction, scattering, and absorption efficiencies from two silver cylinders of different size: Fig. 2(a), $a=60$ nm and Fig. 2(b), $a=200$ nm. The particle is isolated either in water or in vacuum, and the illumination is done with a plane monochromatic *P*-polarized wave. One observes a plasmon resonance maximum in both cylinder samples. The intensity of the line-shape peak is similar, and

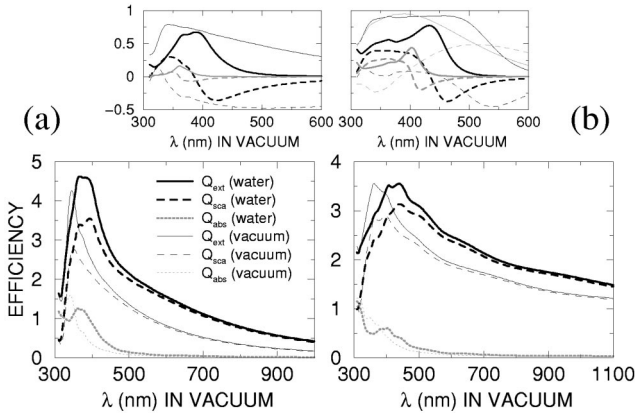

FIG. 2. Extinction (Q_{ext}), scattering (Q_{sca}), and absorption (Q_{abs}) efficiencies from an isolated silver cylinder of radius either $a=60$ nm, (a); or $a=200$ nm, (b). The particle is immersed either in water or in vacuum. Top figures: real (solid lines) and imaginary (broken lines) parts of the external *P*-polarization Mie coefficients (versus wavelength in vacuum) for the cylinder in water; (a) Dark thin lines: $n=1$, dark thick lines: $n=2$, gray thick lines: $n=3$. (b) Dark thin lines: $n=4$, dark thick lines: $n=5$, gray thin lines: $n=1$, gray thick lines: $n=6$. The incidence is done with a *P*-polarized plane wave.

even 30% higher from the smaller particle. Top figures show the behavior of the external field Mie coefficients versus vacuum wavelength (*P* polarization), for the cylinder in water, which contribute most to build the surface-plasmon resonance. The n coefficient expresses the multipolar order of contribution to the scattered field. The Mie coefficients exhibit both a change of sign in their imaginary part and an enhancement of their real part when a Mie resonance is matched.[35] While morphology-dependent resonances in dielectric particles, are labeled with the l number, which determines the number of internal intensity radial peaks, in metallic particles $l=1$, since there is field outside the particle, and the only peak intensity in the radial direction is placed at the surface.

The position of the particle resonances in the spectrum depends on the wavelength, geometrical configuration, and materials of the system. However, as shown in Refs. 29–31, the presence of an interface slightly shifts, weakens and broadens them. An evanescent incident wave on the cylinder enhances these efficiencies as it better couples with the cylinder eigenmodes. This is so because the contribution of higher multipolar orders of the field to the scattering cross section are enhanced with this kind of incidence.[28] It is observed that the immersion of the particle in water not only red shifts the efficiencies (compared to those in air) but even enhances them.

Plasmon resonances in metallic particles are not so efficiently excited as morphology-dependent resonances in nonabsorbing high refractive index dielectric particles (eg., see Refs. 29,30) under incident evanescent waves. The distance from the particle to the surface must be very small to avoid the evanescent wave decay, normal to the propagation direction along the surface.

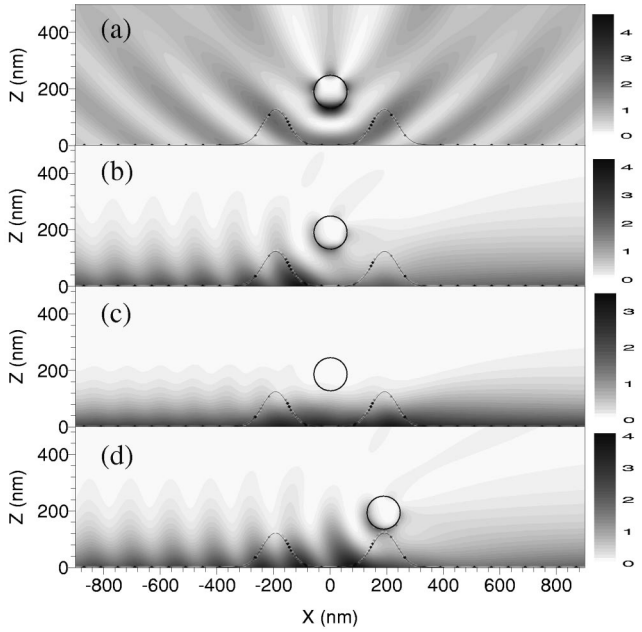

FIG. 3. $|H/H_o|^2$, *P* polarization, from a silver cylinder with $a=60$ nm immersed in water, on a glass surface with defect parameters $X_0=191.4$ nm, $h=127.6$ nm, and $\sigma=63.8$ nm, at distance $d=132.6$ nm. Gaussian beam incidence with $W=4000$ nm. (a) $\lambda=387$ nm (on resonance), $\theta_o=0°$. (b) $\lambda=387$ nm (on resonance), $\theta_o=66°$. (c) $\lambda=316$ nm (off resonance), $\theta_o=66°$. (d) $\lambda=387$ nm (on resonance), $\theta_o=66°$. The cylinder center is placed at (0, 192.6) nm in (a), (b), and (c), and at (191.4, 192.6) nm in (d).

A. Very small cylinders

In Fig. 3, we plot the near-field intensity distribution $|H/H_0|^2$ corresponding to the configuration of Fig. 1. A silver cylinder of radius $a=60$ nm scans at constant distance $d=162.6$ nm above the interface. The system is illuminated by a *P*-polarized Gaussian beam ($W=4000$ nm) at $\theta_0=0°$ and $\lambda=387$ nm ($\epsilon_2=-3.22+i0.70$). The surface protrusions are positioned at $X_0=\pm 191.4$ nm with height $h=127.6$ nm and $\sigma=63.8$ nm. Figure 3(a) shows the aforementioned distribution when the particle is centered between the protrusions. The plasmon resonance is excited as manifested by the field enhancement on the cylinder surface that is higher in its lower portion. At this resonant wavelength, the main Mie coefficient contributor is $n=2$, which can also be deduced from the interference pattern formed along the particle surface: the number of lobes must be $2n$ along this surface.[35] Figure 3(b) shows the same situation but with $\theta_0=66°$. The field intensity close to the particle is higher in Fig. 3(a) because in Fig. 3(b) the distance *d* is large enough to obliterate its better coupling due to the decay of the evanescent wave created by total internal reflection.[29] However, the field intensity is markedly different to the one shown in Fig. 3(c), in which the wavelength has been changed to $\lambda=316$ nm ($\epsilon_2=0.78+i1.07$) so that there is no particle resonance excitation at all. Figure 3(d) shows the same as in Fig. 3(b) but at a different *X* position of the particle. In Fig. 3(c), the interference in the scattered near field due to the presence of the particle is rather weak, the field distribution is now seen to be mainly concentrated at low *z* as an evanescent wave traveling along the interface, and this distribution does not substantially change as the particle moves over the surface at constant *z*. By contrast, in Figs. 3(b) and 3(d) the intensity map is strongly perturbed by the presence of the particle. As we shall see, this is the main reason due to which optical force microscopy is possible at resonant conditions with such small metallic particles used as nanoprobes, and not so efficient at nonresonant wavelengths. It is important to point out in connection with these intensity maps [cf. Figs. 3(b) and 3(d)], the interference pattern at the left side of the cylinder, between the evanescent wave and the strongly reflected waves from the particle, that in resonant conditions behaves as a strong radiating antenna.[29,30,36] This can also be envisaged as due to the much larger scattering cross section of the particle on resonance, hence reflecting backwards higher intensity and thus enhancing the interference with the evanescent incident field. The fringe spacing is $\lambda/2$ (λ being the corresponding wavelength in water). This is explained as follows: The interference pattern formed by the two evanescent waves traveling on the surface opposite to each other, with the same amplitude and no dephasing is proportional to $\exp(-2\kappa z)\cos^2(n_1 k_0 \sin\theta_0 x)$, with $\kappa=(n_1^2\sin^2\theta_0-n_0^2)^{1/2}$. The distance between maxima is $\Delta x=\lambda/(2n_1\sin\theta_0)$. For the angles of incidence used in this work under TIR ($\theta_0=66°$ and 72°), $\sin\theta_0\approx 0.9$, and taking into account the refractive indices of water and glass, this distance can be expressed as $\Delta x\approx\lambda/2n_0$. Δx is similar to the fringe period below the particle in Fig. 3(a), now attributted to the interference between two opposite traveling plane waves: the one transmitted through the interface and the one reflected back from the particle. These intensity structures are, however, better observed for larger particles, as will be shown in Sec. III B.

These near-field interference patterns have previously been shown in Ref. 36, although no interpretation was given there.

Figure 4 shows the near-field plots when the height of the surface defects is inverted ($h=-127.6$ nm) so that they become grooves. In this case, the probe particle can be placed closer to the interface, and thus, we have used a distance $d=15$ nm. As an example the cylinder is placed between both protrusions. Due to the lower distance *d*, the excitation of the plasmon resonance is better in this case. The incidence is done with a *P*-polarized Gaussian beam of $W=4000$ nm. Figure 4(a) shows the same case of normal incidence at the resonant wavelength used previously ($\lambda=387$ nm). Figure 4(b) corresponds to the same situation but at $\theta_0=66°$ (TIR conditions). Figure 4(c) displays the near field when no plasmon resonance is excited ($\lambda=316$ nm) and $\theta_0=66°$, and Fig. 4(d) shows the intensity near field when there is no particle, at $\lambda=316$ nm. Resonance cases [Figs. 4(a) and 4(b)] are recognized because the field is enhanced on the particle surface. Besides, the inteference fringes at the left of the particle exhibit a higher contrast on resonance, as before. This is, again, attributed to the greater scattered power from the particle. Off resonance [Figs. 4(c) and 4(d)], the concentration of intensity field on the dielectric interface reveals the exponential decay along $Z>0$ of the transmitted evanescent wave, traveling along the interface. A standing-wave interference pattern of period $\lambda/2$

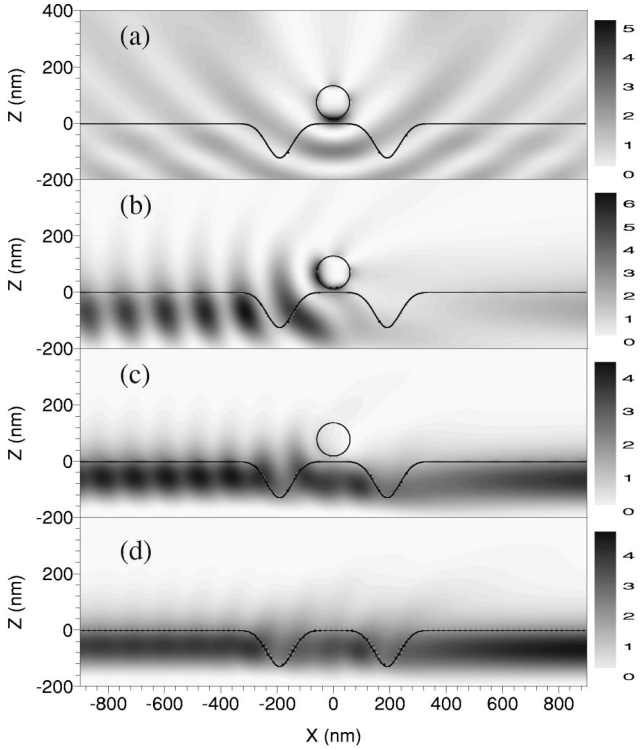

FIG. 4. $|H/H_o|^2$, P polarization, for a silver cylinder with $a=60$ nm immersed in water, on a glass surface with defect parameters $X_0=191.4$ nm, $h=-127.6$ nm, and $\sigma=63.8$ nm, at distance $d=15$ nm. Gaussian beam incidence with $W=4000$ nm. (a) $\lambda=387$ nm (on resonance), $\theta_o=0w°$. (b) $\lambda=387$ nm (on resonance), $\theta_o=66°$. (c) $\lambda=316$ nm (off resonance), $\theta_o=66°$. (d) $\lambda=316$ nm (off resonance), $\theta_o=66°$, no cylinder. The cylinder center is placed at (0, 192.6) nm in (a), (b), and (c).

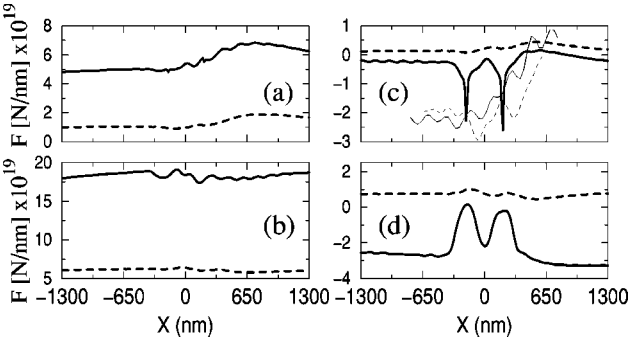

FIG. 5. Force on a silver cylinder with $a=60$ nm immersed in water, scanned at constant distance on a glass surface with defect parameters $X_0=191.4$ nm, and $\sigma=63.8$ nm along OX. The incident field is a P-polarized Gaussian beam with $W=4000$ nm and $\theta_0=66°$. (a) Horizontal force, $h=127.6$ nm, $d=132.6$ nm. (b) Horizontal force, $h=-127.6$ nm, $d=15$ nm. (c) Vertical force, $h=127.6$ nm, $d=132.6$ nm. (d) Vertical force, $h=-127.6$ nm, $d=15$ nm. Solid curves: $\lambda=387$ nm (on resonance), broken curves: $\lambda=316$ nm (off resonance). Thin lines in (c) show $|H/H_0|^2$ (in arbitrary units), averaged on the perimeter of the cylinder cross section, while it scans the surface. The actual magnitude of the intensity in the resonant case is almost seven times larger than in the nonresonant one.

is observed, as explained before, at the left of the grooves and even in the space between them, due to reflection of this surface wave by both the particle and defects [Fig. 4(c)] and more weakly by the defects alone [Fig. 4(d)]. For $Z<0$ in Figs. 4(c) and 4(d) there is an interference pattern between the incident field and that reflected downward by the dielectric interface. The field inside these protrusions is lower than outside. The first minimum of this intensity pattern along the X direction in the lower medium appears in the bottom of Figs. 4(c) and 4(d).

Figure 5 shows the variation of the Cartesian components of the electromagnetic force [F_X, Figs. 5(a) and 5(b); F_Z, Figs. 5(c) and 5(d)] on scanning the particle at constant distance d above the interface, at either plasmon resonance excitation ($\lambda=387$ nm, solid lines), or off resonance ($\lambda=316$ nm, broken lines). The incident-beam power (per unit length) on resonance is 3.9320×10^{-9} W/nm, and 3.9327×10^{-9} W/nm at $\lambda=316$ nm. Figures 5(a) and 5(c) show the force when $h=127.6$ (protrusions) and $d=132.6$ nm. On the other hand, Figs. 5(b) and 5(d), display the force when $h=-127.6$ (grooves) and $d=15$ nm. The incidence is done with a P-polarized Gaussian beam of $W=4000$ nm at $\theta_0=66°$. It is seen from these curves that the force distributions resembles the surface topography on resonant conditions with a signal that is remarkably larger than off resonance. This feature is specially manifested in the Z component of the force, in which the two protrusions are clearly distinguished from the rest of interference ripples, as explained above. Figure 5(c) also shows (thin lines) the scanning that conventional near-field microscopy would measure in this configuration, namely, the normalized magnetic near-field intensity, averaged on the cylinder cross section. These intensity curves are shown in arbitrary units, and in fact the curve corresponding to plasmon resonant conditions is almost seven times larger than the one off resonance. The force curves show, on one hand, that resonant conditions also enhance the contrast of the surface topography image. Thus, the images obtained from the electromagnetic force follows more faithfully the topography than that from the near-field intensity. This is a fact that we have also observed with other profiles, including surface-relief gratings. Figures 5(b) and 5(d) show some results for h inverted, namely, the interface profile of Fig. 4, then the vertical component of the force distribution presents the inverted contrast. Notice that in Figs. 5(b) and 5(d) the particle is closer to the surface, $d=15$ nm, thus giving a higher image contrast. On the whole, we observe from these results that both the positions and sign of the defect height can be distinguished by the optical force scanning.

For comparison, we show in Fig. 6 the same configurations as in Fig. 5 but for a silicon cylinder. Top figures show the efficiencies (with the same plot code as in Fig. 2) versus the wavelength in vacuum. The peaks now corresponds to morphology-dependent resonances, which are not red shifted when the particle is immersed in water with respect to air, as occurred for the plasmon resonances of silver particles. This is so because the resonances in dielectric particles depend on their geometry more strongly than in metallic particles. The peak contrast when the cylinder is in water, however, dimin-

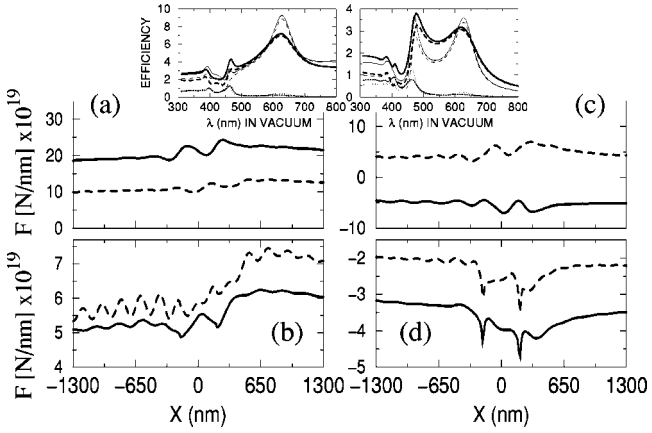

FIG. 6. Force on a silicon cylinder with $a=60$ nm immersed in water, on a glass surface with defect parameters $X_0=191.4$ nm, $\sigma=63.8$ nm, and $h=127.6$ nm scanned at distance $d=132.6$. The incident field is a Gaussian beam with $W=4000$ nm and $\theta_0=66°$. (a) Horizontal force, *S* polarization. (b) Horizontal force, *P* polarization. (c) Vertical force, *S* polarization. (d) Vertical force, *P* polarization. Solid curves: $\lambda=638$ nm (on resonance), broken curves: $\lambda=538$ nm (off resonance). Top figures show the extinction (solid lines), scattering (broken lines) and absorption (dotted lines) efficiencies versus the wavelength in vacuum for an isolated silicon cylinder of radius $a=60$ nm. Thick lines: cylinder in water, thin lines: cylinder in vacuum. Left top figure: *S* polarization, right top figure: *P* polarization. The incidence is done with a plane wave.

ishes. Its position in the spectrum of course is not altered by the kind of incidence. These morphology-dependent resonant peaks are slightly shifted, weakened and broadened by the presence of a surface. Incidence with an evanescent wave enhances the resonance peak, like as stated previously for the silver particle efficiencies, and shown in Refs. 29,30. Figures 6(a) and 6(c) show the horizontal and vertical forces, respectively, for an incident *S*-polarized Gaussian beam with $W=4000$ nm at $\theta_0=66°$, and Figs. 6(b) and 6(d) plot the same forces for an incident *P*-polarized Gaussian beam with the same W and θ_0. The incident-beam power (per unit length) is 9.0755×10^{-9} W/nm on *S*-polarization resonance, 3.9281×10^{-9} W/nm on *P*-polarization resonance, 9.0796×10^{-9} W/nm at $\lambda=538$ nm, *S* polarization, and 3.9299×10^{-9} W/nm at $\lambda=538$ nm, *P* polarization. The force signals in the vertical components of the force again reveal the structure of the surface topography. This is remarkable in *P* polarization, and more poorly exhibited in *S* polarization, in which the contrast is worse and not substantially improved when the particle resonance is excited. The resonant wavelength $\lambda=638$ nm ($\epsilon_2=14.99+i0.14$) excites the ($n=0,l=1$) eigenmode for *P* polarization, and the ($n=1,l=1$) eigenmode for *S* polarization. At $\lambda=538$ ($\lambda=17.03+i0.40$) there is no resonance excitation (see the top figures in Fig. 6) for both polarizations.

We have also simulated a scanning of the silicon particle when the surrounding medium is air. Under these conditions, the morphology-dependent resonances are more enhanced than before because of the larger index contrast between the particle and the external medium (see top figures in Fig. 6). The angle of incidence has now been chosen in order to

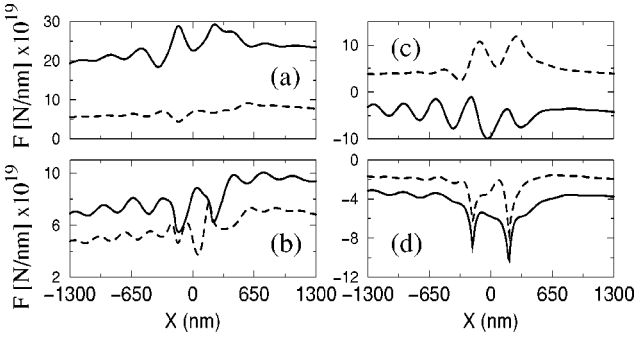

FIG. 7. Same as Fig. 6 but for the cylinder immersed in air and $\theta_0=44.90°$. This angle of incidence has been chosen in order to reproduce the same exponential decay of the evanescent wave (transmitted into the upper medium) as in the conditions of Fig. 6. The critical angle now is $\theta_c=41.14°$. The field intensity at the upper interface boundary has also been normalized so as to be the same as in Fig. 6.

reproduce the same exponential decay of the evanescent field as in Fig. 6. This incidence angle is $\theta_0=44.90°$, (the critical angle in the configuration air/water is $\theta_c=41.14°$). Besides, the intensity field at the upper boundary interface line has been normalized so as to get the same transmitted intensity as in the case of no particle and flat interface. The incident-beam power (per unit length) required is 7.3591×10^{-9} W/nm on *S*-polarization resonance, 3.9976×10^{-9} W/nm on *P*-polarization resonance, 7.3599×10^{-9} W/nm at $\lambda=538$ nm, *S* polarization and 3.9980×10^{-9} W/nm $\lambda=538$ nm, *P* polarization. Figure 7 shows the force distribution from this scanning (the configuration is exactly the same as in Fig. 6). Qualitatively, the behavior of the force is the same as previously, but its strength is greater, as expected. The *Z* component in *P* polarization presents a higher contrast compared to that in water. In *S* polarization, however, the contrast remains practically the same, and the oscillatory pattern does not actually reveal the topography of the surface.

To finish this comparison between the force signals from silicon and silver cylinders, we must say that the ratio d/λ is smaller in the cases shown for the silicon particle, because the wavelengths used in these cases are larger and while d remains the same in nanometers. Thus, the evanescent field incident on the particle is greater in this case, this however does not improve the force signal, as has been shown.

B. Larger cylinders

In this section, we address a cylinder with radius $a=200$ nm. Since this size is comparable to the wavelength, the multiple scattering with the surface increases, and the presence of a resonance also enhances the intensity around the particle.[29,30] This also affects the force signal obtained with these larger particles, as shown next.

Figure 8 displays near-field intensity maps. Figure 8(a) corresponds to $\theta_0=0°$ and a resonant wavelength $\lambda=441$ nm ($\epsilon_2=-5.65+i0.75$). The particle being placed on the left of both protrusions. Figure 8(b) corresponds to $\theta_0=66°$ (TIR illumination conditions), at the same resonant

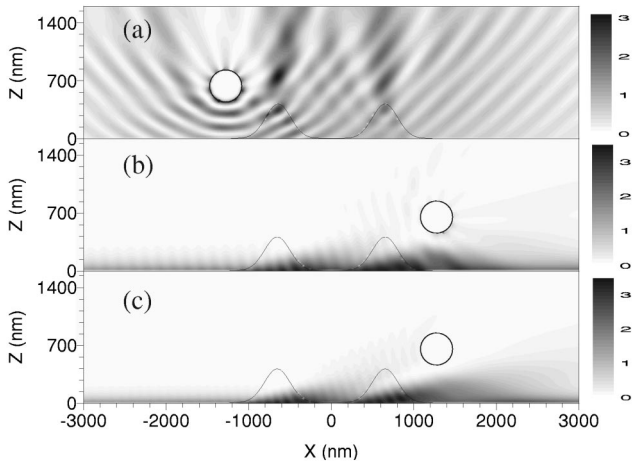

FIG. 8. $|H/H_o|^2$ for P polarization for a silver cylinder with $a=200$ nm immersed in water, on a glass surface with parameters $X_0=638$ nm, $h=425.3$ nm, and $\sigma=212.7$ nm, at distance $d=442$ nm. Gaussian beam incidence with $W=4000$ nm. (a) $\lambda=441$ nm (on resonance), $\theta_o=0°$ and the cylinder center placed at $(-1276,642)$ nm. (b) $\lambda=441$ nm (on resonance), $\theta_o=66°$ and the cylinder center placed at (1276,642) nm. (c) $\lambda=316$ nm (off resonance), $\theta_o=66°$ and the cylinder center placed at (1276,642) nm.

wavelength, the particle now being on the right of the protrusions. Figure 8(c) corresponds to $\theta_0=66°$ (TIR incidence), at the no resonant wavelength $\lambda=316$ nm ($\epsilon_2=0.78+i1.07$), the particle being placed at the right of the protrusions. The incident beam is P polarized with $W=4000$ nm. The surface protrusions are positioned at $X_0=\pm 638$ nm with height $h=425.3$ nm and $\sigma=212.7$ nm. All the relevant size parameters are now comparable to the wavelength, and hence to the decay length of the evanescent wave. That is why now the plasmon resonance cannot be highly excited. When no resonant wavelength is used, the intensity interference fringes due to the presence of the particle are weaker. On the other hand, Fig. 8(a) shows the structure of the near field scattered under $\theta_0=0°$. There are three objects that scatter the field: the two protrusions and the particle. They create an inteference pattern with period $\lambda/2$ (with λ being the wavelength in water). Besides, the particle is showing an inteference pattern around its surface due to the two counterpropagating plasmon waves that circumnavigate it.[29,30] The number of lobes along the perimeter is nine, which reflects that the contribution to the field enhancement at this resonant wavelength comes from Mie's coefficients $n=5$ and $n=4$ [see top Fig. 2(b)]. Figure 8(b) shows the weaker excitation of the same plasmon resonance under TIR conditions. Now, it is also patent, like in Sec. III A), the interference pattern at the incident side of the configuration. This pattern has again a period $\lambda/2$ (λ being the wavelength in water). If nonresonant illumination conditions are used, the particle is too far from the surface to substantially perturb the transmitted field, then the intensity of the transmitted evanescent field remains closely attached to the interface, and is scattered by the surface protrusions. The field felt by the particle in this situation is not sufficient to

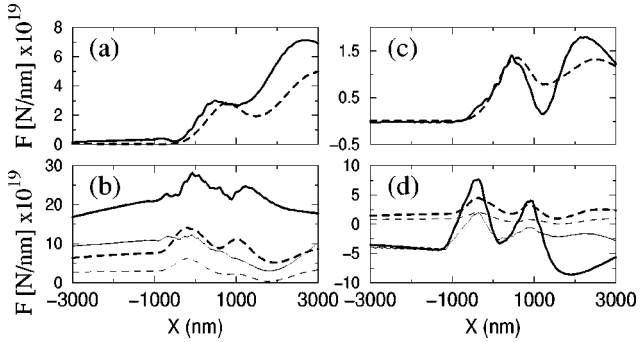

FIG. 9. Force on a silver cylinder with $a=200$ nm immersed in water, scanned at constant distance on a glass surface with parameters $X_0=638$ nm and $\sigma=212.7$ nm along OX. The incident field is a P-polarized Gaussian beam with $W=4000$ nm and $\theta_0=66°$. (a) Horizontal force, $h=425.3$, $d=442$ nm. (b) Horizontal force, $h=-425.3$, $d=25$ nm. (c) Vertical force, $h=425.3$, $d=442$ nm. (d) Vertical force, $h=-425.3$, $d=25$ nm. Solid curves: $\lambda=441$ nm (on resonance), broken curves: $\lambda=316$ nm (off resonance). Thin solid curves: $\lambda=441$ nm (on resonance) at $\theta_0=72°$, thin broken curves: $\lambda=316$ nm (off resonance) at $\theta_0=72°$.

yield a well-resolved image of the surface topography, as shown next for this same configuration.

Figure 9 shows the components of the force [F_X, Figs. 9(a) and 9(b); F_Z, Figs. 9(c) and 9(d)] for either plasmon excitation conditions ($\lambda=441$ nm, solid lines), or off resonance ($\lambda=316$ nm, broken lines) as the cylinder scans at constant distance d above the surface. Figures 9(a) and 9(c) show the image yielded by the force distribution when $h=425.3$ (protrusions) and $d=442$ nm, and Figs. 9(b) and 9(d), when $h=-425.3$ (grooves) and $d=25$ nm. The incidence is done with a P-polarized Gaussian beam of $W=4000$ nm at either $\theta_0=66°$ (thick curves) or $\theta_0=72°$ (thin curves). The incident-beam power (per unit length) is 3.9313×10^{-9} W/nm on resonance and 3.9327×10^{-9} W/nm at $\lambda=316$ nm when $\theta_0=66°$, and 3.9290×10^{-9} W/nm on resonance and 3.9315×10^{-9} W/nm at $\lambda=316$ nm when $\theta_0=72°$. As before, resonant conditions provide a better image of the surface topography making the two protrusions distinguishable with a contrast higher than the one obtained without plasmon excitation. The surface image corresponding to the force distribution is better when the protrusions are inverted [Figs. 9(b) and 9(d)] because then the particle can be kept closer to the interface. Again, the curve contrast yielded by protrusions and grooves is inverted from each other. The positions of the force distribution peaks corresponding to the protrusions now appear appreciably shifted with respect to the actual protrusions' position. This shift is explained as due to the Goos-Hänchen effect of the evanescent wave.[27] We observe that the distance between these peaks in the F_Z curve is aproximately $2X_0$. This shift is more noticeable in the force distribution as the probe size increases.[37] Again, the F_Z force distribution has a higher contrast at the (shifted) position of the protrusions. The force signal with these bigger particles is larger, but the probe has to be placed farther from the surface at constant height scanning. This affects the strength of the signal (compare top and bottom curves). Finally, it is important to state

that the angle of incidence (supposed larger than the critical angle θ_c) influences both the contrast and the strength of the force: thin curves show in Figs. 9(b) and 9(d) as an example, that the contrast decreases as the angle of incidence increases. At the same time, the strength of the force signal also diminishes.

As seen in the force figures for both sizes of particles, most curves contain tiny ripples. They are due to the field intensity interference pattern as shown in Figs. 3, 4, and 7, and discussed above. As the particle moves, the force on it depends on these oscillations. As a matter of fact, it can be noted in the force curves that these tiny ripples are mainly present at the left side of the particle, where the interference takes place.

It is worth remarking, however, that these oscillations are less marked in the force distribution (cf. their tiny ripples), than in the near-field intensity distribution, where the interference patterns present much higher contrast.

IV. DISCUSSION

A. On the attractive and repulsive nature of the vertical forces

The horizontal forces acting on the cylinder are scattering forces due to radiation pressure of both the incident evanescent wave and the field scattered by the protrusions, thus the forces are positive in all the cases studied. As for the vertical forces, two effects are competing for determining its sign. First, is the influence of the polarizability,[24,25] which depends on the polarization of the illumination. On the other hand, it is well known that an evanescent wave produces only gradient forces in the vertical direction. For silver cylinders, the force at wavelength $\lambda = 387$ ($\epsilon_2 = -3.22 + i0.70$) and at $\lambda = 441$ nm ($\epsilon_2 = -5.65 + i0.75$) must be attractive, while at $\lambda = 316$ nm ($\epsilon_2 = 0.78 + i1.07$), the real part of the polarizability changes its sign, and so does the gradient force, thus becoming repulsive (on cylinders, as here of not a very large size). However, in the cases studied in this work, not only the multiple scattering of light between the cylinder and the flat portion of the interface, but also the surface defects produce scattered waves both propagating (into $Z > 0$) and evanescent under TIR conditions. Thus, scattering forces are also taking place in the Z component of the force. This affects the sign of the forces but it is more remarkable as the size of the objects increases. In larger cylinders and defects (cf. Fig. 9), the gradient force is weaker than the scattering force thus making F_Z to become repulsive on scanning at $\lambda = 441$ nm (plasmon excited). On the other hand, for the smaller silver cylinders studied (cf. Figs. 5–7), the gradient force is greater than the scattering force at $\lambda = 387$ nm (plasmon excited) and thus the force is attractive in this scanning. Also, as the distance between particle and surface decreases, the gradient force becomes more attractive.[24,25] This explains the dips and change of contrast in the vertical force distribution on scanning both protrusions and grooves. At $\lambda = 316$ nm (no plasmon excited), both scattering and gradient forces act cooperatively in the vertical direction making the force repulsive, no matter the size of the cylinder. For the silicon cylinder shown, the vertical forces acting under TIR conditions are attractive in absence of surface interaction (for both polarizations and the wavelengths used). However, this interaction is able to turn into repulsive the vertical force for S polarization at $\lambda = 538$ nm, due to the scattering force.

This study also reveals the dependence of the attractive or repulsive nature of the forces on the sizes of the objects (probe and defects of the surface), apart from the polarizability of the probe and the distance from the interface, when illumination under total internal reflection is considered. The competition between the strength of the scattering and the gradient force determines this nature.

B. On the order of magnitude of the forces

We wish to point out that the order of magnitude of the forces obtained in 2D calculations of this work is consistent with that of forces in experiments and 3D calculations of Refs. 13–25. Suppose a truncated cylinder with axial length $L = 10$ μm, and a Gaussian beam with $2W \sim 10$ μm. Then, a rectangular section of $L \times 2W = 10^2$ μm^2 is illuminated on the interface. For an incident power $P_0 \sim 1$ mW, spread over this rectangular section, the incident intensity is $I_0 \sim 10^{-2}$ mW/μm^2, and the force range from our calculations is $F \sim 10^{-14} - 10^{-13}$ N. Thus, the forces obtained in Figs. 9(b) and 9(d) are consistent with those presented, for example, in Ref. 17.

V. CONCLUSIONS

In this paper, we have studied the transduction of optical forces felt by a probe particle on scanning a dielectric interface.

Comparing with dielectric particles, we conclude that the optical force signal for metallic probes is, under resonant conditions (plasmon excitation on the metallic particle), stronger. However, when the surface protrusions are large, the excitation of the plasmon resonance is not so efficient compared to those morphology-dependent resonances of dielectric particles, and the resulting force image has less contrast than with dielectric probes.[27] The force signal neatly reveals the topography of the surface. This is mainly achieved with the vertical component of the force. Besides, this signal improves the one obtained by known near-field microscopy techniques. When the size of both the defects on the surface and the probe increases, the results are more dramatic: the plasmon resonance is more difficult to excite (owing to the distance from the flat portion of the surface to the probe), but the force exhibits the same behavior with smaller scales only shifting the corresponding force peaks' positions with respect to the ones of the surface protrusions. Silicon particles provide an image with a less contrast. This contrast is only weakly improved when morphology-dependent resonances are excited on the probe, but it is not greater than the one obtained with silver probes under plasmon resonance excitation. The calculation shows, however, that the image is better when the silicon particle is placed in air, than when it is immersed in water. This is so due to the better excitation of these morphological resonances when the index contrast between the particle and the surrounding medium is higher.

Finally, when the angle of incidence increases (supposed larger than the critical angle), both the contrast of the images and the strength of the forces diminish in all cases. The averaging process involved in Maxwell's stress tensor and the local character of the force in contrast with that of the electromagnetic field, avoid the near-field interference and artifacts contained in the near-field intensity distribution.

ACKNOWLEDGMENTS

This research was supported by Ministerio de Educación y Cultura of Spain. A grant of J. R. Arias-González from Comunidad Autónoma de Madrid, as well as partial support from Dirección General de Investigación Científica y Técnica and the European Union are also acknowledged.

*Corresponding author. Email address: mnieto@icmm.csic.es

[1] A. Ashkin, J.M. Dziedzic, J.E. Bjorkholm, and S. Chu, Opt. Lett. **11**, 288 (1986).
[2] K. Sasaki, M. Koshioka, H. Misawa, N. Kitamura, and H. Masuhara, Opt. Lett. **16**, 1463 (1991).
[3] H. Misawa, K. Sasaki, M. Koshioka, N. Kitamura, and H. Masuhara, Appl. Phys. Lett. **60**, 310 (1992).
[4] H. Misawa, M. Koshioka, K. Sasaki, N. Kitamura, and H. Masuhara, J. Appl. Phys. **70**, 3829 (1991).
[5] J. Hotta, K. Sasaki, H. Masuhara, and Y. Morishima, J. Phys. Chem. B **102**, 7687 (1998).
[6] A. Pralle, M. Prummer, E.-L. Florin, E.H.K. Stelzer, and J.K.H. Hörber, Microsc. Res. Tech. **44**, 378 (1999).
[7] A. Pralle, E.-L. Florin, E.H.K. Stelzer, and J.K.H. Hörber, Appl. Phys. A: Mater. Sci. Process. **A66**, S71 (1998).
[8] S.B. Smith, Y. Cui, and C. Bustamante, Science **271**, 795 (1996).
[9] A. Ashkin and J.M. Dziedzic, Appl. Phys. Lett. **24**, 586 (1992).
[10] K. Svoboda and S.M. Block, Opt. Lett. **19**, 13 (1994).
[11] K. Sasaki, J. Hotta, K. Wada, and H. Masuhara, Opt. Lett. **25**, 1385 (2000).
[12] E.-L. Florin, J.K.H. Hörber, and E.H.K. Stelzer, Appl. Phys. Lett. **69**, 446 (1996).
[13] M. Ohtsu, S. Jiang, T. Pangaribuan, and M. Kozuma, in *Near Field Optics*, Vol. 242 of *NATO Advanced Study Institute, Series E: Applied Sciences*, edited by D. W. Pohl and D. Courjon (Kluwer, Dordrecht, The Netherlands, 1993).
[14] *Forces in Scanning Probe Methods*, Vol. 286 of *NATO Advanced Study Institute, Series E: Applied Sciences*, edited by H.-J. Güntherodt, D. Anselmetti, and E. Meyer (Kluwer, Dordrecht, The Netherlands, 1995).
[15] F. Depasse and D. Courjon, Opt. Commun. **87**, 79 (1992).
[16] T. Sugiura and S. Kawata, Bioimaging **1**, 1 (1993).
[17] S. Kawata and T. Sugiura, Opt. Lett. **17**, 772 (1992).
[18] A. Dereux, C. Girard, O.J.F. Martin, and M. Devel, Europhys. Lett. **26**, 37 (1994).
[19] C. Girard, A. Dereux, and O.J.F. Martin, Phys. Rev. B **49**, 13 872 (1994).
[20] E. Almaas and I. Brevik, J. Opt. Soc. Am. B **12**, 2429 (1995).
[21] L. Novotny, R.X. Bian, and X.S. Xie, Phys. Rev. Lett. **79**, 645 (1997).
[22] B. Hecht, H. Bielefeldt, L. Novotny, Y. Inouye, and D.W. Pohl, Phys. Rev. Lett. **77**, 1889 (1996).
[23] K. Okamoto and S. Kawata, Phys. Rev. Lett. **83**, 4534 (1999).
[24] P.C. Chaumet and M. Nieto-Vesperinas, Phys. Rev. B **62**, 11 185 (2000).
[25] P.C. Chaumet and M. Nieto-Vesperinas, Phys. Rev. B **61**, 14 119 (2000).
[26] M. Lester and M. Nieto-Vesperinas, Opt. Lett. **24**, 936 (1999).
[27] M. Lester, J.R. Arias-González, and M. Nieto-Vesperinas, Opt. Lett. **26**, 707 (2001).
[28] M. Quinten, A. Pack, and R. Wannemacher, Appl. Phys. B: Lasers Opt. **68**, 87 (1999).
[29] J.R. Arias-González and M. Nieto-Vesperinas, J. Opt. Soc. Am. A **18**, 657 (2001).
[30] J.R. Arias-González and M. Nieto-Vesperinas, Opt. Lett. **25**, 782 (2000).
[31] J.R. Arias-González, M. Nieto-Vesperinas, and A. Madrazo, J. Opt. Soc. Am. A **16**, 2928 (1999).
[32] A. Madrazo, J.R. Arias-González, and M. Nieto-Vesperinas, Opt. Commun. **162**, 91 (1999).
[33] A. Madrazo and M. Nieto-Vesperinas, J. Opt. Soc. Am. A **14**, 1859 (1997).
[34] J. A. Stratton, *Electromagnetic theory* (McGraw-Hill, New York, 1941).
[35] J.F. Owen, R.K. Chang, and P.W. Barber, Opt. Lett. **6**, 540 (1981).
[36] J.R. Krenn, A. Dereux, J.C. Weeber, E. Bourillot, Y. Lacroute, J.P. Goudonnet, G. Schider, W. Gotschy, A. Leitner, F.R. Aussenegg, and C. Girard, Phys. Rev. Lett. **82**, 2590 (1999).
[37] For a better picture of this shift, see the grating case in Ref. 27.